RSC Advances

PAPER

View Article Online
View Journal | View Issue

Cite this: *RSC Adv.*, 2017, **7**, 7130

Selective catalytic reduction of NO with NH_3 over Mo–Fe/beta catalysts: the effect of Mo loading amounts†

Jianlin Deng,‡[a] Jixing Liu,‡[a] Weiyu Song,‡[a] Zhen Zhao,[a] Liang Zhao,[a] Huiling Zheng,[a] Alex Chinghuan Lee,[b] Yongsheng Chen[b] and Jian Liu*[a]

Received 22nd November 2016
Accepted 15th January 2017

DOI: 10.1039/c6ra27126j

www.rsc.org/advances

A series of Mo_x–Fe/beta catalysts with constant Fe and variable Mo content were synthesized and investigated for selective catalytic reduction (SCR) of NO_x with NH_3. It was found that the $Mo_{0.2}$–Fe/beta catalyst exhibited excellent activity, N_2 selectivity and preferable resistance to H_2O and SO_2. The Mo_x–Fe/beta catalysts were characterized by various analytical techniques. TEM and SEM images showed that the addition of Mo could enhance the dispersion of iron oxides. The results of NH_3-TPD and Py-IR indicated that the introduction of Mo resulted in a change of Brønsted acidity, which was associated with high-temperature SCR activity. XPS and XANES results showed that the introduction of Mo resulted in a change of Fe^{2+} content, which determined the low-temperature activity. DFT calculations showed the strong effects of Mo on the crystal structure, charge distribution and oxygen vacancy formation energy of iron oxides, which further explained the role of Mo in the catalyst behaviors during the SCR process.

1. Introduction

Nitrogen oxides such as NO, NO_2 and N_2O_5 (NO_x), originating from mobile and stationary sources, have been a major kind of air pollution. Due to numerous environmental issues (*e.g.* acid rain, photo chemical smog, ozone depletion and greenhouse effect) and serious harm to human health resulting from NO_x, stringent regulations and great efforts have been made to confine NO_x emissions.[1,2] Nowadays, selective catalytic reduction with ammonia (NH_3-SCR) is regarded as one of the most effective technologies for the removal of NO_x.[3]

In recent years, zeolite-based catalysts promoted by transition metals have attracted much attention for NH_3-SCR.[4,5] Different zeolite materials, such as MOR,[6] MFI,[7] CHA,[8] and beta[9] loaded with various transition metals have been investigated extensively on the SCR of NO with NH_3. Among these zeolite-based catalysts, Fe-based catalysts exhibited excellent activity as an attractive candidate for SCR reaction.[10,11] He *et al.*[12] reported Fe-ZSM5 catalysts exhibited a fine low-temperature activity, and conclude that Fe^{2+} species are the active sites for NH_3-SCR. Nedyalkova *et al.*[13] suggested that the presence of Fe^{2+} should promote the NH_3-SCR reaction at low temperatures. Further, they proposed that the capability of Fe^{2+} to interact with NO should be a key for high NH_3-SCR activity at low temperatures. On the other hand, Long *et al.*[14] suggested that Fe^{3+} should enhance oxidation of NO to NO_2 and thus increase SCR activity at high temperature. Devadas *et al.*[15] showed that the role of Fe^{3+} was to oxidize NO to NO_2 at the high temperature, which was the rate-determining step for NH_3-SCR. The presence of Fe^{3+} species could effectively decrease the unwanted NH_3 unselective oxidation at high temperatures, resulting in high N_2 selectivity.[16] It can be conclude that Fe^{3+} species play a crucial role on NH_3-SCR activity at high temperature. For Fe/beta catalysts, Fe^{2+} and Fe^{3+} have been found on the surface of catalysts as redox couple. It is difficult to enhance Fe^{2+} and Fe^{3+} loading amounts at same time, when the total Fe amounts in the catalyst are fixed. Thus, only narrow activity temperature window can be achieved for single iron-based zeolite catalysts.[11] A study from Kobayashi *et al.*[17] showed WO_3–TiO_2 catalysts possess a larger surface area and higher Brønsted acidity with the increasing of WO_3 loading. WO_3–TiO_2 catalysts exhibit higher SCR activity at high temperatures, which is mainly attributed to the higher Brønsted acidity. Thus, Brønsted acidity is another factor on the high-temperature performance of NH_3-SCR reaction. It is viable to introduce an extra metal ion to regulate the Fe^{2+} content and Brønsted acidity, which can further enhance catalytic activity of Fe-based catalysts from low to high temperature.

Molybdenum has been proved to be a promoter to enhance the surface acidity and the amount of active sites, and it has been widely used for oxide catalysts. For example, Liu *et al.*[18]

[a]*State Key Laboratory of Heavy Oil Processing, Beijing Key Lab of Oil & Gas Pollution Control, China University of Petroleum, 18# Fuxue Road, Chang Ping District, Beijing 102249, P. R. China. E-mail: liujian@cup.edu.cn; Fax: +86-10-69724721; Tel: +86-10-89732278*

[b]*Department of Mechanical and Automation Engineering, The Chinese University of Hong Kong, Shatin, New Territories, Hong Kong SAR, P.R. China*

† Electronic supplementary information (ESI) available. See DOI: 10.1039/c6ra27126j

‡ These authors contributed equally as the first author.

reported that the role of MoO_3 is to promote the formation of Brønsted acidity, which contributes to the adsorption and activation of NH_3 on the catalyst surface, resulting in the higher activity of Ce–MoO_3/TiO_2. Ding *et al.*[19] proposed that the addition of Mo inhibit the growth of CeO_2 particle size, improve the redox ability and increase the amount of surface acidity. It is favorable for the improvement of NH_3-SCR performance.

In the present study, beta zeolite supported constant iron content and variable molybdenum amounts were prepared by a successive incipient-wetness impregnation. It was found that the addition of Mo showed a noticeable promoting effect on the activity of Fe/beta for NH_3-SCR reaction at a wide temperature range. The effect of Mo on morphology of catalysts, Brønsted acidity and Fe^{2+} content was thoroughly studied. Furthermore, DFT calculations illustrate that the introduction of Mo results in the variation of Fe valence and affects the oxidation of NO to NO_2. At the microscopic level, the interaction of iron and molybdenum, the oxygen vacancy formation energy and electronic properties of catalyst have been also investigated.

2. Experiment and calculation details

2.1 Catalyst preparation

Mo_x–Fe/beta catalysts were prepared by a successive incipient-wetness impregnation method using H-beta zeolite as the support. The synthesis method of H-beta was described in ESI.† In a typical synthesis, it was performed by mixing H-beta powders with appropriate amount of $Fe(NO_3)_3$ solution and treated in ultrasound for 4 h at room temperature. The precursor was dried at 110 °C for 12 h. Then, the samples were calcined at 500 °C for 5 h in the static air atmosphere and denoted as Fe/beta. The loading amounts of Fe for Fe/beta were maintained at 3% wt. Finally, Mo_x–Fe/beta catalysts with different Mo loading amounts were synthesized by the same method using $(NH_4)_6Mo_7O_{24}\cdot 4H_2O$ as the precursor and Fe/beta as the support. (x represents the weight percentage of Mo to beta, x = 0.1, 0.2, 0.5 and 1). For comparison, $Mo_{0.2}$/beta catalyst were also synthesized by the same method using $(NH_4)_6Mo_7O_{24}\cdot 4H_2O$ as the precursor and beta as the support.

2.2 Catalyst characterization

Powder X-ray diffraction (XRD) pattern was recorded on a Bruker D8 advance system with Cu K_α (λ = 0.15406 nm) radiation at 40 kV and 10 mA in the 2θ range of 5–70°.

The surface morphology of the catalyst was collected by field emission scanning electron microscopy (FESEM) on a Quanta 200F instruments using accelerating voltages of 5 kV, in combination with an EDAX genesis 4000 energy-dispersive X-ray spectrometer (EDX).

The element content of as-prepared materials was determined by a Varian 715-ES inductively coupled plasma-atomic emission spectrometer (ICP-AES).

Transmission electron microscopy (TEM) micrographs were performed on a JEOL JEM-F20 electron microscope equipped with a field emission source operating at 200 kV. The average particle diameter was calculated from the mean diameter frequency distribution with the formula: $d = \sum n_i d_i / \sum n_i$. Where, n_i is the number of particles with particle diameter d_i in a certain range. The elemental local and mapping analyses were recorded by energy dispersive spectroscopy (EDS) using a Tecnai F20 electron microscope.

Temperature-programmed desorption of ammonia (NH_3-TPD) measurement was carried out on a conventional flow apparatus. Prior to measurement, 0.1 g of sample was pretreated in N_2 gas (30 mL min^{-1}) at 600 °C for 0.5 h and then cooled down to room temperature. Next, the sample was exposed to a mixed gas (10% NH_3/N_2) flow of 30 mL min^{-1} for 0.5 h to ensure the sufficient adsorption of NH_3. Before desorption, the sample was flushed in N_2 gas for 1.5 h. Subsequently, NH_3 desorption was performed in the range of 100–700 °C at a heating rate of 10 °C min^{-1} under a N_2 flow of 30 mL min^{-1}.

Pyridine-IR analysis was performed on a MAGNAIR 560 FT-IR instrument. The sample was dehydrated at 500 °C for 4 h under a vacuum of 1.3×10^{-3} Pa, followed by adsorption of pyridine vapor at room temperature and evacuated at different temperatures.

Temperature programmed reduction of hydrogen (H_2-TPR) experiment was carried out in a home-made apparatus. Prior to reduction, the sample (50 mg) was treated from room temperature to 600 °C under a flow rate of 30 mL min^{-1} N_2 and then cooled down to 60 °C in a purging N_2 flow. The temperature programmed reduction process was performed in 30 mL min^{-1} flow of 10% H_2/N_2 at a ramp rate of 10 °C min^{-1} up to 900 °C.

X-ray photoelectron spectroscopy (XPS) experiment was conducted on a PerkinElmer PHI-1600 ESCA spectrometer equipped with Mg K_α ($h\nu$ = 1253.6 eV) radiation. The binding energy was determined referenced to the C 1s peak of contaminant carbon (BE = 284.6 eV).

X-ray absorption near edge structure (XANES) spectra at Fe L3-edge (706.8 eV) were recorded in total electron yield mode on the BL27SU Beamline at Spring-8 in Japan.

2.3 Catalyst activity evaluation

Catalyst activity tests were conducted on a fixed-bed quartz micro-reactor at atmospheric pressure. The gas compositions were as follows: 500 ppm NO, 500 ppm NH_3, 3 vol% O_2, balance N_2 and the gas flow rate was 500 mL min^{-1}. The concentration of NO_x (NO_x = NO + NO_2) in the inlet and outlet gas at steady-state was measured using a flue gas analyzer (Model-4000VM, SIGNAL international Ltd., UK), and NH_3 and N_2O was monitored by a NEXUS 670-FTIR spectrometer. NO_x conversion was calculated according to the following equation (eqn (1)).

$$NO_x \text{ conversion} = \frac{[NO_x]_{inlet} - [NO_x]_{outlet}}{[NO_x]_{inlet}} \times 100\% \quad (1)$$

N_2 selectivity in SCR reaction was calculated by eqn (2)

$$N_2 \text{ selectivity} = \left(1 - \frac{2[N_2O]_{outlet}}{[NO_x]_{inlet} + [NH_3]_{inlet} - [NO_x]_{outlet} - [NH_3]_{outlet}}\right) \times 100\% \quad (2)$$

2.4 Calculational details

DFT calculations were performed with the PBE (Perdew–Burke–Ernzerhof)[20] function using the Vienna *Ab Initio* Simulation Package (VASP).[21] The spin-polarized calculations were performed. The projector augmented wave method (PAW) was used to describe the interaction between the ions and the electrons with the frozen-core approximation.[22] The kinetic energy cutoff was 400 eV. All structures were relaxed until the forces acting over each atom were smaller than 0.05 eV $Å^{-1}$ and electronic energies were converged within 10^{-4} eV. Owing to the 3d Fe electrons, hematite is a strongly correlated system in which Fe d- and O p-orbitals hybridize significantly. DFT has a strong tendency to delocalize d electrons, resulting in the underestimation of the band gap in metal oxides.[23] The U and J terms describing the Coulomb and exchange interactions are always combined together in the form $U_{eff} = U - J$. The U_{eff} value ($U_{eff} = 3.8$) and bulk lattice parameter ($a = b = 5.107$ Å and $c = 13.959$ Å) are used.[24]

Hematite (α-Fe_2O_3) has a corundum-type structure, and is the most stable and abundant iron oxide. Previous experimental and theoretical results reveal that Fe terminated Fe_2O_3 (001) surface is the inherently most stable surface,[25–27] which indicates that Fe terminated Fe_2O_3 (001) surface is the most probably exposed in the supported catalysts. Top and side view of Fe terminated Fe_2O_3 (001) surface are shown in Fig. S1a and b,† respectively. To achieve perfect stoichiometry, we use a 15-layer slab. The 9 top-layer slabs of the surface are allowed to relax while the other layers beneath the surface are frozen. The repeated slabs are separated from their neighboring images by a 12 Å-width vacuum in the direction perpendicular to the surface. We use the primitive rhombohedral unit cell of Fe_2O_3 with the magnetic configuration (+ − − +) to build Fe terminated surface slab, which is previously proved to be the most favored magnetic configuration for α-Fe_2O_3 in energy.[28] The calculated magnetic charge density of Fe terminated Fe_2O_3 (001) surface shows in Fig. S2.† To test the accuracy of our computational setup, we compared the mesh of k-points ($2 \times 2 \times 1$ and $3 \times 3 \times 1$), and the energy difference was less than 0.02 eV. Thus, the $2 \times 2 \times 1$ mesh of k-points is adopted in this calculation.

3. Results

3.1 NH_3-SCR performance

NO_x reduction reactions over pure H-beta, Mo/beta, Fe/beta and Mo_x–Fe/beta catalysts were examined at the flow rate of 500 mL min^{-1} using the feeding gas containing 500 ppm NO, 500 ppm NH_3 and 3% O_2 in the range of 100–600 °C. It can be seen from Fig. 1a that NO_x conversion changes with the increasing of reaction temperature. For H-beta, the maximum NO_x conversion is only 50% in the whole temperature range. For Mo/beta catalysts, NO_x conversion increases to approximately 70% at 500 °C. However, Fe/beta catalyst exhibits superior activity than Mo/beta and H-beta. With the introduction of Mo, the activity temperature window of Mo_x–Fe/beta catalysts at maximum NO_x conversion changes. It can be seen that the temperature window of Fe/beta catalyst at maximum NO_x conversion is 275–425 °C. For $Mo_{0.2}$–Fe/beta catalysts, the temperature range has been enlarged to 250–475 °C. Obviously, the addition of Mo influences the activity temperature window of Mo_x–Fe/beta catalysts, and $Mo_{0.2}$–Fe/beta catalyst exhibits the widest temperature

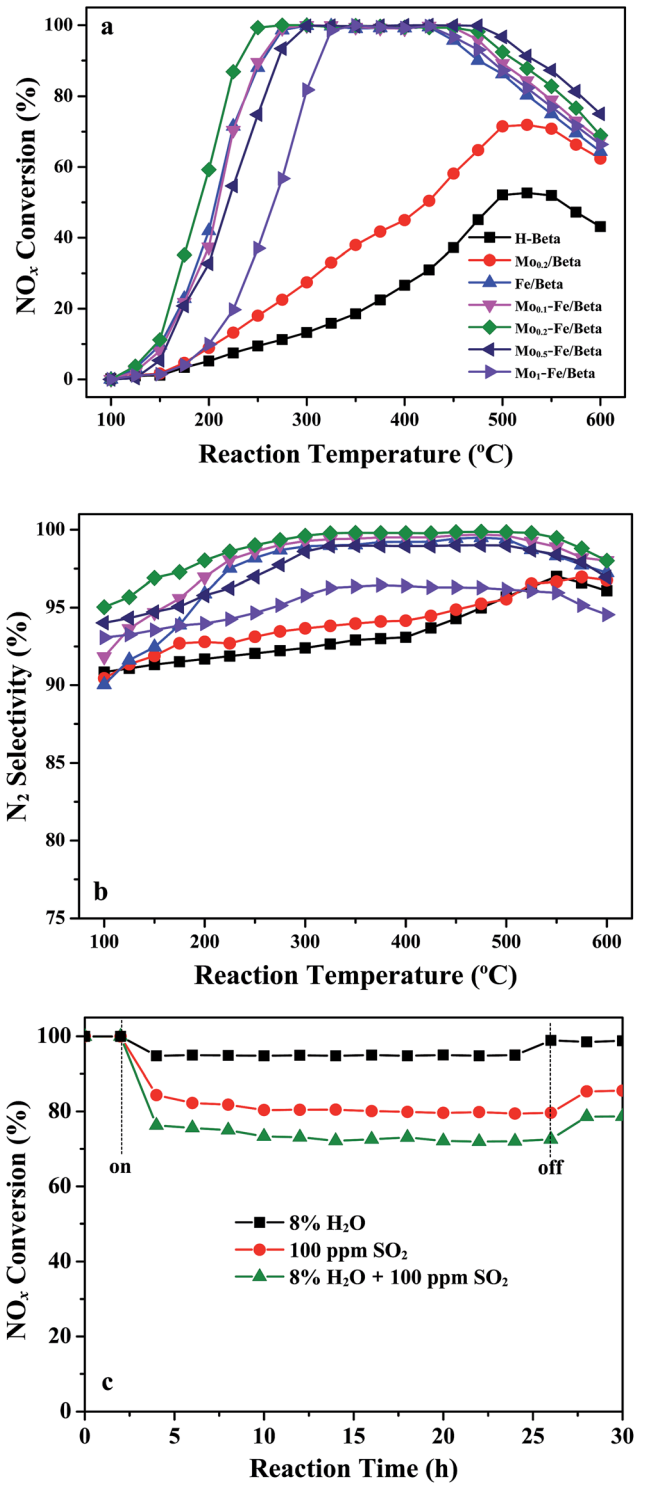

Fig. 1 NO_x conversion (a) and N_2 selectivity (b) as a function of reaction temperature over pure H-beta, Mo/beta, Fe/beta and Mo_x–Fe/beta catalysts with variable Mo loading amounts in the temperature range of 100–600 °C. (c) NO_x conversion in the presence of H_2O and/or SO_2 over $Mo_{0.2}$–Fe/beta catalyst at 300 °C.

window. $Mo_{0.5}$–Fe/beta catalysts exhibit favorable high-temperature activity. $Mo_{0.2}$–Fe/beta catalysts show the best low-temperature activity. Fig. 1b illustrates that the low-temperature (100–300 °C) N_2 selectivity of catalysts is also influenced by the addition of Mo. When Mo loading amounts increased from 0 to 0.2% wt, the low-temperature N_2 selectivity of Mo_x–Fe/beta catalysts increased gradually. Once Mo loadings exceed 0.2% wt, the low-temperature N_2 selectivity of catalysts begins to fall. However, the high-temperature (above 425 °C) N_2 selectivity of Fe/beta, $Mo_{0.1}$–Fe/beta, $Mo_{0.2}$–Fe/beta and $Mo_{0.5}$–Fe/beta are almost unchanged. The high-temperature N_2 selectivity of Mo_1–Fe/beta decreases remarkably. NO_x conversion begins to decrease above 425 °C due to the declining NH_3 absorptivity and the unselective oxidation of NH_3. These results clearly demonstrate that the appropriate amount of Mo is beneficial to improving NH_3-SCR activity and broadening the temperature window.

With regard to the actual use of lean SCR catalysts, sulfur and H_2O are important factors that could cause the deactivation of catalysts. The effect of SO_2 and H_2O on the NO_x conversion over $Mo_{0.2}$–Fe/beta catalyst at 300 °C is displayed in Fig. 1c. The sample was continuously exposed to feeding gas containing 100 ppm SO_2 and 8% H_2O for 30 h, respectively. It can be seen that the initial NO_x conversion is about 100% and keeps steady within 2.5 h without SO_2 and H_2O. When only H_2O is added to the feed gas, NO_x conversion decreases slightly and is maintained 95% for 20 h. The SCR activity can recover when H_2O is shut off, indicating that $Mo_{0.2}$–Fe/beta catalyst is not sensitive to H_2O. The slight inhibiting effect is mainly attributed to the competitive adsorption of H_2O and NH_3 molecule on the acid sites.[29,30] When only SO_2 is present in the feed gas, the conversion of NO_x decreases obviously, but it is still above 80% and keeps steady for 20 h. When SO_2 is shut off, the SCR activity rises again, but can not reach the initial level. However, the conversion of NO_x decreases severely under the coexistence of both SO_2 and H_2O. The reason may be the deposition of ammonium sulfate on the surface of the catalysts which can block the active sites.[30,31] NO_x conversion can still be maintained at approximately 75% during the reaction period. After the removal of SO_2 and H_2O, NO_x conversion can be restored to about 80%. The above results suggest that $Mo_{0.2}$–Fe/beta catalyst shows moderate resistance to sulfur and preferable H_2O tolerance.

3.2 The results of XRD

XRD results (Fig. 2) exhibit that the characteristic peaks of all these samples are corresponding to beta zeolite, indicating that the original zeolite structure remains intact. In addition, no diffraction peaks corresponding to α-Fe_2O_3 (PDF #33-0644) and MoO_3 (PDF #35-0609) crystalline phases are displayed among all catalysts, indicating that iron and molybdenum species were well dispersed on the surface of beta support as amorphous oxides. Iron and molybdenum species were well dispersed on the surface of beta support as amorphous oxides, or aggregated into minicrystals, which too small to be detected by XRD. The following SEM and TEM characterization will give particular structure information.

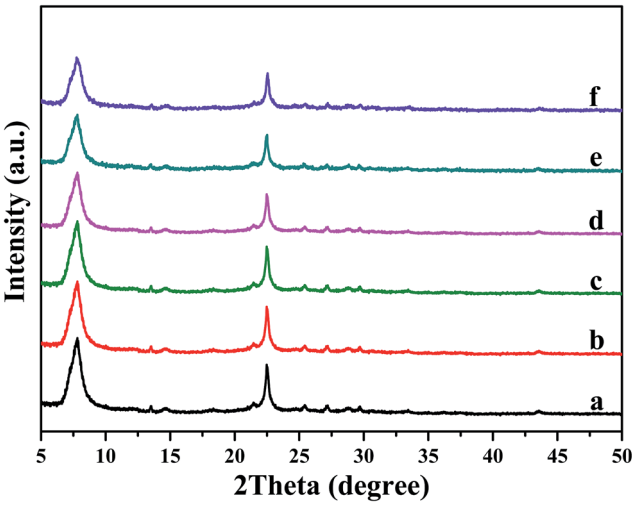

Fig. 2 XRD patterns of pure H-beta (a); Fe/beta (b); $Mo_{0.1}$–Fe/beta (c); $Mo_{0.2}$–Fe/beta (d); $Mo_{0.5}$–Fe/beta (e); Mo_1–Fe/beta (f).

3.3 The results of SEM

SEM was carried out to further insight into the change of the morphology induced by the loading of Mo. Fig. 3a shows SEM image of pure H-beta, which is composed of egg-like aggregates with diameter around 150 nm. No obviously change in the morphology of zeolite is observed after the incorporation of iron and molybdenum. With the introduction of Fe and Mo (Fig. 3b and c, respectively), H-beta grain surfaces are rougher by covered with a "layer". EDX results collected from different regions (Point 1 and Point 2 in Fig. 3b; Point 3 and Point 4 in Fig. 3c) exhibit similar compositions. The average iron loadings of 2.87–2.94% wt are detected for Fe/beta and $Mo_{0.2}$–Fe/beta samples (Table 1), in good agreement with the initial nominal loading amounts. Moreover, no molybdenum element is detected for the $Mo_{0.2}$–Fe/beta sample. It should be due to the fact that the actual Mo loading is much lower than the detection limit. The Mo contents, determined *via* ICP-AES technique, are 0.07% wt, 0.12% wt, 0.43% wt and 0.87% wt in quality percentage for $Mo_{0.1}$–Fe/beta, $Mo_{0.2}$–Fe/beta $Mo_{0.5}$–Fe/beta and Mo_1–Fe/beta, respectively.

3.4 The results of TEM

TEM images and the size distributions of supported molybdenum and iron species were further studied by HAADF-STEM characterization combining with EDS element-mapping analysis. Fig. 4a shows HAADF-STEM images of $Mo_{0.2}$–Fe/beta together with the elemental mapping images for O, Al, Si, Fe and Mo in the same region. From elemental mapping image of Mo and Fe, it is clearly seen that Mo and Fe species are highly dispersed on the supports. For Fe/beta (Fig. 4b) catalyst, the faintback ground belongs to beta zeolite and the dark spots are Fe oxide nanoparticles. However, the presence of Fe oxide was not detected by XRD due to the small size of the crystallites and their high dispersion. It's noted that the average particle size for Fe oxides significantly decreased from 4.28 nm for Fe/beta to 3.44 nm for $Mo_{0.2}$–Fe/beta (Fig. 4d) with the increasing of Mo

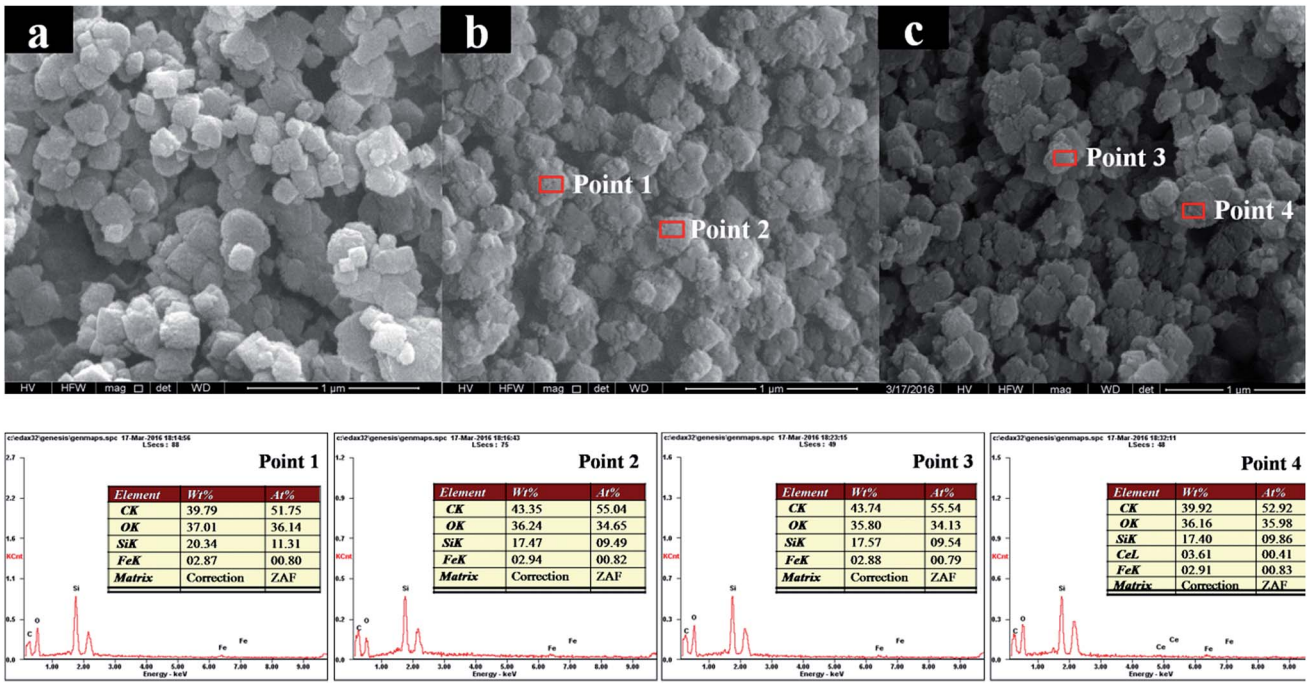

Fig. 3 SEM images and EDX analysis for pure H-beta (a); Fe/beta (b); $Mo_{0.2}$–Fe/beta (c).

Table 1 Surface and bulk composition and oxidation state of Mo 3d and Fe 2p species over Mo_x–Fe/beta catalysts from XPS analysis

Samples	Mo[b]	Mo/Si[a]	Fe[b]	Fe^{2+}/Fe^{3+}[a]
Fe/beta	—	—	2.85%	0.62
$Mo_{0.1}$–Fe/beta	0.07%	0.17%	2.96%	0.72
$Mo_{0.2}$–Fe/beta	0.12%	0.36%	2.86%	0.83
$Mo_{0.5}$–Fe/beta	0.43%	0.91%	2.91%	0.58
Mo_1–Fe/beta	0.83%	1.05%	2.84%	0.44

[a] As determined by XPS analysis. [b] As determined by ICP-AES analysis.

loading amount. It indicates that the addition of Mo could increase the dispersion of Fe species, which played an important role in determining the extent of NO_x conversion in the NH_3-SCR. However, the average particle size of Fe oxide nanoparticles on Mo_1–Fe/beta (3.96 nm Fig. 4e) insignificantly grew larger compared with $Mo_{0.2}$–Fe/beta. It can be inferred that proper amount of Mo addition is beneficial to the dispersion of Fe species and the activity of catalysts.

3.5 The results of TPD

Temperature-programmed desorption of ammonia was performed to determine the catalyst surface acidity. Fig. 5 shows NH_3-TPD profiles of pure H-beta, Fe/beta and Mo_x–Fe/beta catalysts. A low-temperature peak (peak L) and a high temperature peak (peak H) can be observed for all samples. The former one is assigned to physically adsorbed NH_3 or ammonium species adsorbed at the weak acid sites. The latter one is attributed to NH_3 strongly adsorbed at the Brønsted acid sites.[32] It could be seen peak L has lager area and shifts to high temperature with the addition of Fe, indicating that new Lewis acids sites form on the Fe sites. The peak H slightly shifts to higher temperature with the increasing of Mo contents from 0 to 0.5%, indicating that Brønsted acidity strengthen gradually. However, the peak H of Mo_1–Fe/beta catalysts obviously shifts to low temperature. The reason is that the excess of Mo aggregates and results in the decrease of Brønsted acidity.

3.6 The results of Py-IR

Fig. 6 depicts Py-IR spectra of Fe/beta and Mo_x–Fe/beta catalysts after outgassing at specific temperature. In general, the typical bands from pyridine adsorption related to Lewis acid sites (L) can be observed at around 1450 cm^{-1}, while the presence of Brønsted acid sites (B) can be seen at around 1540 cm^{-1}.[30] As shown in Fig. 6A, the bands at 1540 and 1636 cm^{-1} can be assigned to C–N stretching of pyridine ions to Brønsted acid sites, while the bands at 1450 and 1607 cm^{-1} can be assigned to the vibration of pyridine physically adsorbed to Lewis acid sites. The band at 1488 cm^{-1} is attributed to both B and L acid sites.[30,33,34] The intensity of all the bands in Fig. 6B dramatically decreases compared with that in Fig. 6A, indicating that less NH_3 can be adsorbed at high temperature than that at low temperature. The quantitative results of acid amount obtained from Py-IR measurement at 200 and 350 °C are summarized in Table 2. The amounts of Brønsted acid sites increase significantly with the introduction of Mo. $Mo_{0.5}$–Fe/beta catalysts have the most abundant acid sites among all the catalysts. The excess amounts of Mo (0.1% wt) have a negative effect on the surface acid sites of the catalysts.

3.7 The results of H_2-TPR

The results of H_2-TPR experiments are displayed in Fig. 7. H_2-TPR profile of α-Fe_2O_3 is also shown and there are four

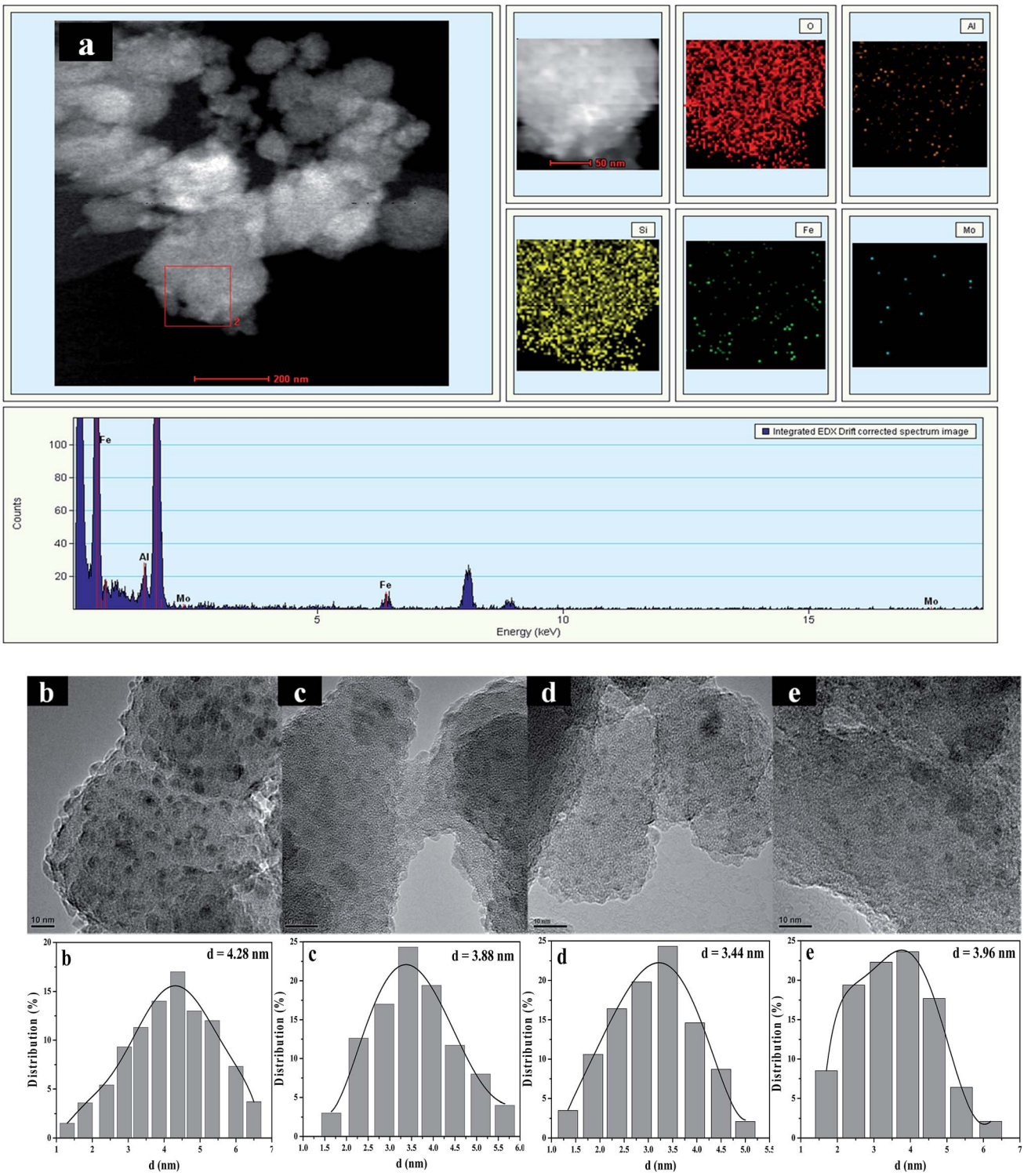

Fig. 4 HAADF-STEM image and EDS elemental mapping (a) of $Mo_{0.2}$–Fe/beta catalyst. TEM images, and size distribution of Fe oxide or/and Mo oxide nanoparticles of Fe/beta (b); $Mo_{0.1}$–Fe/beta (c); $Mo_{0.2}$–Fe/beta (d); Mo_1–Fe/beta (e).

reduction features between 300–900 °C. The peak centered at 380 °C could be attributed to the reduction of Fe^{3+} to Fe^{2+}. The peak at around 600 °C and 700 °C correspond to the reduction of Fe_3O_4 to FeO and FeO to Fe, respectively. The reduction peak centered at about 792 °C is ascribed to the reduction of Fe^{2+} to Fe^0.[35] A new reduction peak appeared at around 515 °C for Fe/beta and Mo_x–Fe/beta catalysts, which could be due to the direct reduction of Fe_3O_4 to Fe.[36] The reduction temperature of Fe^{3+} species firstly decreases with the introduction of Mo ($Mo_{0.2}$–Fe/beta < $Mo_{0.1}$–Fe/beta < Fe/beta), which is attributed to

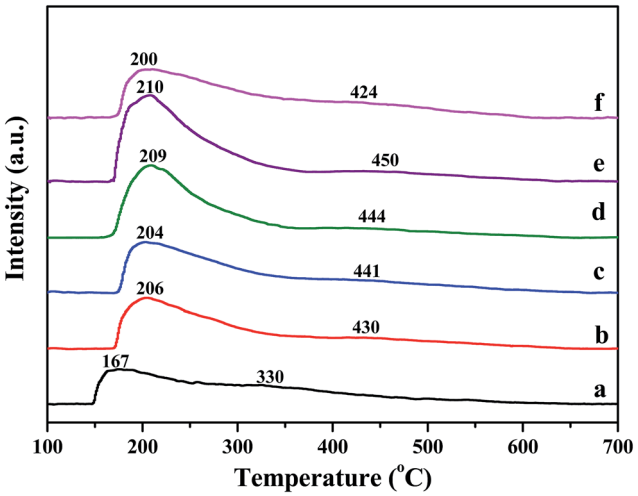

Fig. 5 NH_3-TPD curves of pure H-beta (a); Fe/beta (b); $Mo_{0.1}$–Fe/beta (c); $Mo_{0.2}$–Fe/beta (d); $Mo_{0.5}$–Fe/beta (e); Mo_1–Fe/beta (f).

the weakening of the Fe–O bond due to the incorporation of Mo. However, with increasing of Mo loading amounts from 0.2 to 1.0% wt, the reduction peak shifts to high temperature. This shows that the excess amount of Mo reduces the redox property of Fe species and the activity of the catalyst.

3.8 The results of XPS

XPS results of Fe 2p for Fe/beta and Mo_x–Fe/beta catalysts are shown in Fig. 8. Peaks located near 711.5 and 710 eV can be assigned to Fe^{3+} and Fe^{2+}, respectively.[12] The results from deconvolution are presented in Table 1. It is noted that Fe^{2+} content increases with the introduction of Mo and reaches the maximum when Mo content is 0.2% wt. With further increasing of Mo, Fe^{2+} content remarkably decreases. The reason can be explained that the surface of Fe_2O_3 is covered by a large number of MoO_3, which makes it difficult to form oxygen vacancy. A more detailed explanation will be provided based on the DFT calculations in the following sections.

Table 2 Physicochemical properties of Mo_x–Fe/beta catalysts obtained from Py-IR spectroscopy

	200 °C (μmol g^{-1})		350 °C (μmol g^{-1})	
Samples	L	B	L	B
Fe/beta	81	74	45	29
$Mo_{0.1}$–Fe/beta	77	80	48	31
$Mo_{0.2}$–Fe/beta	82	82	47	36
$Mo_{0.5}$–Fe/beta	83	97	52	39
Mo_1–Fe/beta	72	86	48	35

3.9 The results of XANES

X-ray absorption near edge spectroscopy (XANES) was further performed in total electron yield mode. The samples were mixed with graphite powders to increase electric conductivity and minimize charging effect. Fe L_3-edge XANES spectra of the samples are shown in Fig. 9. Two absorption peaks are observed at 706.8 eV (A_1) and 708.8 eV (A_2). The splitting feature of Fe L_3 edge comes from the interplay of crystal field, spin-orbital and electronic interaction.[37] Based on the charge transfer multiplet theory,[38] the peaks at 706.8 and 708.8 eV correspond to the $2p_{3/2}$ 3d electron transition for Fe^{2+} and Fe^{3+}, respectively. The energy locations are consistent with the results reported by Yang.[39] Furthermore, the intensity ratios of $A_1/(A_1 + A_2)$ for (a) Fe/beta, (b) $Mo_{0.2}$–Fe/beta, (c) $Mo_{0.5}$–Fe/beta are estimated to be 0.45, 0.49 and 0.38, respectively. The results show comparable quantity both Fe^{2+} and Fe^{3+} states coexist in all the samples. Specifically, $Mo_{0.2}$–Fe/beta catalysts exhibit the maximum Fe^{2+} amounts, which is in agreement with XPS results.

3.10 DFT calculations

In this work, XRD and SEM results show that the original beta zeolite structure is not destroyed with the addition of Fe and Mo. Additionally, H-beta catalysts show rather inferior activity in NH_3-SCR compared with Fe/beta and Mo_x–Fe/beta catalysts. Therefore, it is reasonable that beta zeolite is shown to be as the support and Fe_2O_3 model is used to

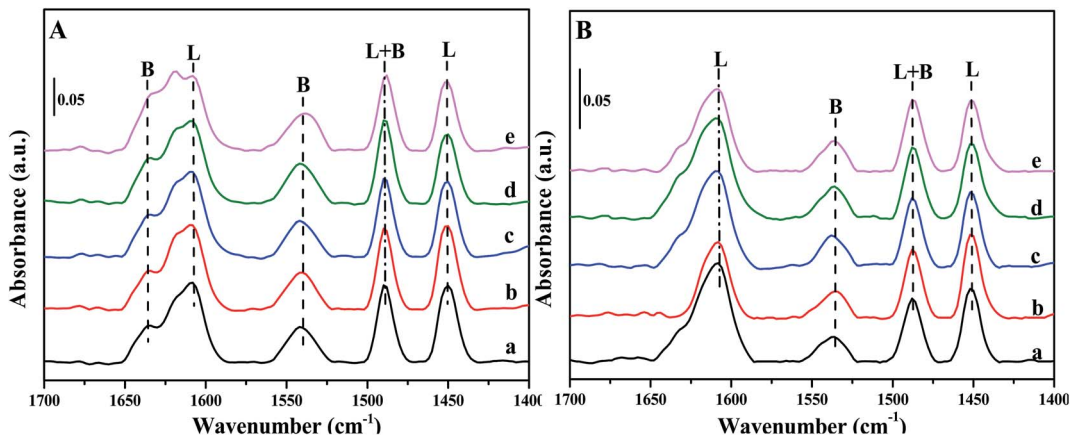

Fig. 6 FT-IR spectra of pyridine adsorbed on Fe/beta (a); $Mo_{0.1}$–Fe/beta (b); $Mo_{0.2}$–Fe/beta (c); $Mo_{0.5}$–Fe/beta (d); Mo_1–Fe/beta (e) after degassing at 200 °C (A) and 350 °C (B).

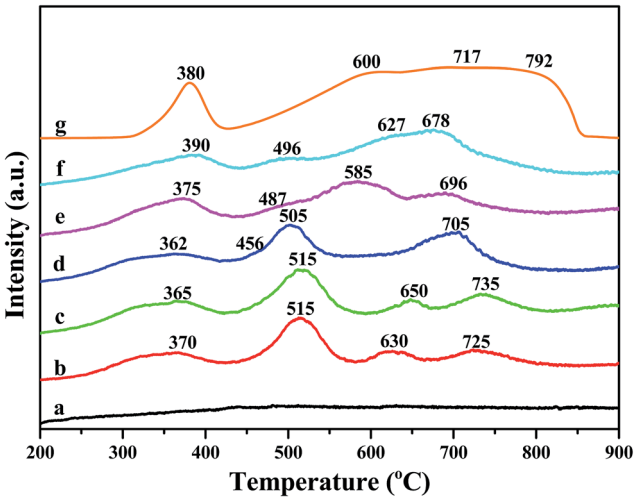

Fig. 7 H_2-TPR profiles of H-beta (a); Fe/beta (b); $Mo_{0.1}$–Fe/beta (c); $Mo_{0.2}$–Fe/beta (d); $Mo_{0.5}$–Fe/beta (e); Mo_1–Fe/beta (f); α-Fe_2O_3 (g).

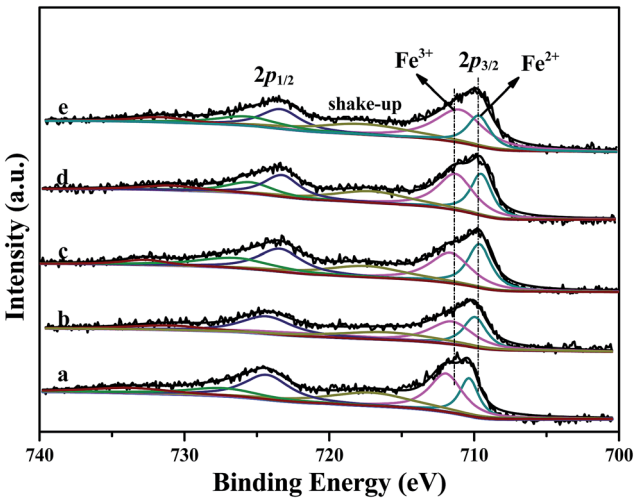

Fig. 8 XPS results of Fe 2p of Fe/beta (a); $Mo_{0.1}$–Fe/beta (b); $Mo_{0.2}$–Fe/beta (c); $Mo_{0.5}$–Fe/beta (d); Mo_1–Fe/beta (e).

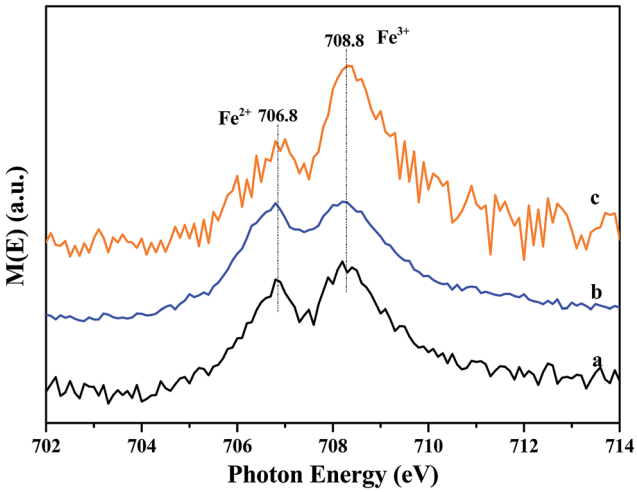

Fig. 9 XANES spectra of the catalysts: Fe/beta (a), $Mo_{0.2}$–Fe/beta (b), $Mo_{0.5}$–Fe/beta (c).

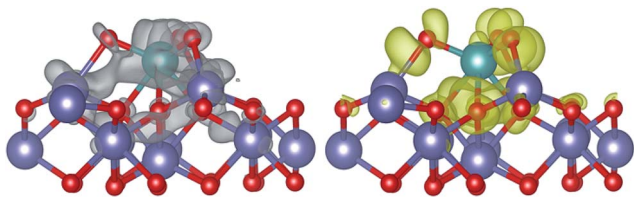

Fig. 10 Charge density difference for MoO_3/Fe_2O_3. The grey and yellow volumes represent zones of electron depletion and accumulation, respectively. Green, red and blue spheres represent Mo, O and Fe atoms, respectively.

represent Fe/beta for simplicity. MoO_3 is considered as the most stable existence form of Mo on the surface of Fe_2O_3 by our calculation. The detailed structure information is shown in Fig. S3 and Table S1,† respectively. The charge density difference plot (Fig. 10) shows that there are strong depletion of electron density around Mo atom and accumulation of electron density between Fe and O atoms, pointing to strong bonding overlap of electrons. The Bader charge we calculated shows significant electron transfer from the Fe_2O_3 to MoO_3 species (0.28 e), which indicates that Mo can interact with the Fe species and enhance the redox ability of the surface of catalysts. The formation energy of an oxygen vacancy (E_{vac}) by DFT calculation is +2.64 eV on the surface of MoO_3/Fe_2O_3, and it is lower than that of pure Fe_2O_3 surface (E_{vac} = 2.97 eV). The results indicate the lattice O atoms are easier to be reduced with the deposition of MoO_3, in accordance with H_2-TPR results. At atomic level, three O atoms of MoO_3 interact with three Fe atoms of the surface of Fe_2O_3 and form three new bonds of Fe–O (bond length: 2.02 Å), which weaken the interaction between Fe and lattice O atom. And the lattice Fe–O bond is elongated from 1.81 Å to 1.83 or 1.84 Å with the deposition of MoO_3. The formation of oxygen vacancy leads to local electrons redistribution. Analysis of calculated Bader charges shows that two Fe atoms on the surface and subsurface in vicinity of oxygen vacancy obtain 0.34 e and 0.38 e, respectively. It indicates the valence of the two Fe atoms transforms from +3 to +2. In other words, the loading of Mo species results in the increase of Fe^{2+} species and the decrease of the Fe^{3+} species, in accordance with the result of the experiment. However, with the loading amounts of Mo increase from 0.2 to 1%, the reduction peak of H_2-TPR shifts to high temperature. In order to interpret aforesaid results, we carried out further theoretical calculations by increasing the number of Mo on the surface of Fe_2O_3. The stable $(MoO_3)_2$ and $(MoO_3)_3$ model was established and the structure was shown in Fig. S4 and S5,† respectively. The calculated E_{vac} are 2.64 and 2.86 eV, respectively. The results indicate E_{vac} of Fe_2O_3 surface increases with the increasing of MoO_3. Therefore the reduction peak of Fe^{3+} species shifts to high temperature in H_2-TPR experiment, when the loading of Mo exceed 0.2% wt.

4. Discussions

With the introduction of Mo, the particle size for Fe oxides and the activity of catalysts change obviously. $Mo_{0.2}$–Fe/beta catalysts exhibit the minimum particle size and favorable SCR performance. It can be concluded that Mo plays an important role in influencing the particle size of iron species and the catalytic performance, which is consistent with previous report.[40] In bimetallic catalysts, the introduction of a second metal is found to suppress the aggregation of monometals.[41] In this work, the smaller iron oxides can exist stably due to the anchor of Mo^{6+} on the iron phase, and then disperse well on the zeolite. However, the average particle size of Fe oxides becomes bigger with the further increasing of Mo loading amounts. It could be due to the formation of crystalline Mo oxides,[42] which fail to disperse Fe species and reduce the activity of catalysts.

NH_3-TPD and Py-IR result show that the strength of Brønsted acidity enhance with an increase of Mo loading. Brønsted acid sites are considered to be associated with Mo–OH groups[41,43] except that on the beta zeolite. However, Brønsted acidity begins to decrease when Mo loading amounts is above 0.5% wt. An obvious variation of Brønsted acidity can be observed: $Mo_{0.5}$–Fe/beta > $Mo_{0.2}$–Fe/beta > $Mo_{0.1}$–Fe/beta > Mo_1–Fe/beta > Fe/beta. The order is in line with that of high-temperature activity. The strong Brønsted acidity results in excellent NH_3 adsorption ability, which is beneficial to improving the high-temperature SCR performance.[44] However, no relation between low-temperature activity and Brønsted acidity is observed. At low temperature more acid sites exist on the surface of catalysts than that at the high temperature. Enough NH_3 can be absorbed and reacts with NO_x to N_2. NH_3 adsorption is not a crucial factor for low-temperature SCR performance. On the other hand, less acid Brønsted acid sites exist on the surface of catalyst at high temperature, indicating that less absorbed NH_3 can participate in NH_3-SCR reaction. Moreover, the part of absorbed NH_3 would also be oxidized to NO_x or decomposed to N_2 at high temperature.[45] Therefore, NH_3 adsorption becomes a rate-limiting step and Brønsted acid sites are responsible for high-temperature activity. $Mo_{0.5}$–Fe/beta exhibits the best high-temperature activity, which is attributed to the highest Brønsted acidity.

Based on H_2-TPR results, Fe^{3+} species are easily reduced to Fe^{2+} when Mo loading amounts reach 0.2% wt, and more oxygen vacancies form on the surface of catalysts simultaneously. This indicates the incorporation of Mo enhances redox property of catalysts. With the further increasing of Mo, the reduction peak of Fe^{3+} species shifts to high temperature. There should be less Fe^{2+} species for $Mo_{0.5}$–Fe/beta and Mo_1Fe/beta catalysts. This is in accordance with the results of XPS and XANES. On the other hand, $Mo_{0.2}$–Fe/beta catalysts possess maximum Fe^{2+} content. Compared with the low-temperature activity in Fig. 1, a similar variation trend can be observed: $Mo_{0.2}$–Fe/beta > $Mo_{0.1}$–Fe/beta > Fe/beta > $Mo_{0.5}$–Fe/beta > Mo_1Fe/beta. It is apparent that superior low-temperature activity is mainly attributed to the higher Fe^{2+} content. Accompanied by the addition of Mo, Fe^{3+} species translate into Fe^{2+} in the vicinity of oxygen vacancy due to the transition of electron. O_2 are adsorbed on the oxygen vacancy and form active chemisorbed oxygen. Chemisorbed oxygen has been considered to be the most active oxygen species and to play an important role in the redox reaction.[30] As for low-temperature NH_3-SCR reaction, the chemisorbed oxygen more easily binds with NO molecule than lattice oxygen to form NO_2.[46] NO oxidation is considered as one of the key reactions in the standard SCR and has been proposed to be the rate determining step in the literature.[47–50] The formed NO_2 species then react with adsorbed NH_3 species on the adjacent Brønsted acid sites to form NH_4NO_3,[51] which further decomposes to N_2 and H_2O. A Langmuir–Hinshelwood mechanism,[52] which considers the NH_3 adsorption on acidic sites and the NO oxidation on Fe sites, is proposed. Therefore, high concentrations of chemisorbed oxygen is beneficial for NO_x reduction due to an increased rate of NO to NO_2 oxidation.[53] $Mo_{0.2}$–Fe/beta catalyst exhibits the best low-temperature performance for the increased oxygen vacancy, which is caused by the introduction of Mo.

5. Conclusions

$Mo_{0.2}$–Fe/beta catalysts exhibit the widest activity temperature window (225–525 °C) at NO_x conversion above 90%. Moreover, $Mo_{0.2}$–Fe/beta catalyst shows moderate resistance to sulfur and preferable H_2O tolerance.

The introduction of Mo can change the amounts of Brønsted acid sites, which may improve the high-temperature performance of Fe/beta catalysts. NH_3-TPD and Py-IR results demonstrate that Brønsted acidity of catalyst surface changes obviously with the increasing of Mo loading amounts.

The addition of Mo influences the dispersion of iron species, and $Mo_{0.2}$–Fe/beta exhibits the minimum average size of Fe oxide particles.

The introduction of Mo has a significant influence on Fe^{2+} content, which is verified by the results of XPS and XANES. The structure of catalyst surface changes due to the interaction of Fe and Mo. More oxygen vacancies and Fe^{2+} are produced on the surface of catalysts, which is beneficial to the low-temperature SCR activity. DFT calculations further illuminate the change of oxygen vacancy formation energy, Fe^{2+} contents and electronic properties.

Acknowledgements

This work was financially supported by the National Natural Science Foundation of China (21673290, 21376261 and 21503273) and 863 Program of China (2015AA034603). The XANES experiments at Spring-8 were, performed on the BL27SU Beamline with the approval of the Japan Synchrotron Radiation Research Institute (JASRI) (Proposal No. 2016A1039).

References

1 S. Brandenberger, O. Kröcher, A. Tissler and R. Althoff, *Catal. Rev.*, 2008, **50**, 492–531.

2 P. Granger and V. Parvulescu, *Chem. Rev.*, 2011, **111**, 3155–3207.
3 J. Li, R. Zhu, Y. Cheng, C. K. Lambert and R. T. Yang, *Environ. Sci. Technol.*, 2010, **44**, 1799–1805.
4 A. M. Beale, F. Gao, I. Lezcano-Gonzalez, C. H. F. Peden and J. Szanyi, *Chem. Soc. Rev.*, 2015, **44**, 7371–7405.
5 J. Dědeček, L. Čapek, P. Sazama, Z. Sobalík and B. Wichterlová, *Appl. Catal., A*, 2011, **391**, 244–253.
6 X. Zhang, Q. Shen, C. He, C. Ma, J. Cheng, L. Li and Z. Hao, *ACS Catal.*, 2012, **2**, 512–520.
7 P. Chen, D. Rauch, P. Weide, S. Schönebaum, T. Simons, M. Muhler, R. Moos and U. Simon, *Appl. Catal., B*, 2014, **148**, 520–531.
8 A. J. O'Malley, I. Hitchcock, M. Sarwar, I. P. Silverwood, S. Hindocha, C. R. A. Catlow, A. P. E. York and P. J. Collier, *Phys. Chem. Chem. Phys.*, 2003, **5**, 3328–3333.
9 N. Liu, R. Zhang, B. Chen, Y. Li and Y. Li, *J. Catal.*, 2012, **294**, 99–112.
10 F. Liu, K. Asakura, H. He, Y. Liu, W. Shan, X. Shi and C. Zhang, *Catal. Today*, 2011, **164**, 520–527.
11 S. Shwan, R. Nedyalkova, J. Jansson, J. Korsgren, L. Olsson and M. Skoglundh, *Ind. Eng. Chem. Res.*, 2012, **51**, 12762–12772.
12 C. He, Y. Wang, Y. Cheng, C. K. Lambert and R. T. Yang, *Appl. Catal., B*, 2009, **368**, 121–126.
13 R. Nedyalkova, S. Shwan, M. Skoglundh and L. Olsson, *Appl. Catal., B*, 2013, **138–139**, 373–380.
14 R. Q. Long and R. T. Yang, *J. Catal.*, 2002, **207**, 224–231.
15 M. Devadas, O. Krocher, M. Elsener, A. Wokaun, G. Mitrikas, N. Soger, M. Pfeifer, Y. Demel and L. Mussann, *Catal. Today*, 2007, **119**, 137–144.
16 F. Liu, H. He, Z. Lian, W. Shan, L. Xie, K. Asakura, W. Yang and H. Deng, *J. Catal.*, 2013, **307**, 340–351.
17 M. Kobayashi and K. Miyoshi, *Appl. Catal., B*, 2007, **7**, 253–261.
18 Z. Liu, S. Zhang, J. Li and L. Ma, *Appl. Catal., B*, 2014, **144**, 90–95.
19 S. Ding, F. Liu, X. Shi, K. Liu, Z. Lian, L. Xie and H. He, *ACS Appl. Mater. Interfaces*, 2015, **7**, 9497–9506.
20 J. P. Perdew, K. Burke and M. Ernzerhof, *Phys. Rev. Lett.*, 1996, **77**, 3865–3868.
21 M. Fuchs and M. Scheffler, *Comput. Phys. Commun.*, 1999, **119**, 67–98.
22 P. E. Blöchl, *Phys. Rev. B: Condens. Matter Mater. Phys.*, 1994, **50**, 17953–17979.
23 A. J. Cohen, P. Mori-Sánchez and W. Yang, *Science*, 2008, **321**, 792–794.
24 X. Huang, S. K. Ramadugu and S. E. Mason, *J. Phys. Chem. C*, 2016, **120**, 4919–4930.
25 M. Lübbe and W. Moritz, *J. Phys.: Condens. Matter*, 2009, **21**, 134010.
26 E. Wasserman, J. R. Rustad, A. R. Felmy, B. P. Hay and J. W. Halley, *Surf. Sci.*, 1997, **385**, 217–239.
27 S. Thevuthasan, Y. J. Kim, S. I. Yi, S. A. Chambers, J. Morais, R. Denecke, C. S. Fadley, P. Liu, T. Kendelewicz and G. E. Brown, *Surf. Sci.*, 1999, **425**, 276–286.
28 L. M. Sandratskii, M. Uhl and J. Kübler, *J. Phys.: Condens. Matter*, 1995, **8**, 983–989.
29 G. Busca, L. Lietti, G. Ramis and F. Berti, *Appl. Catal., B*, 1998, **18**, 1–36.
30 T. Zhang, R. Qu, W. Su and J. Li, *Appl. Catal., B*, 2015, **176–177**, 338–346.
31 K. Wijayanti, K. Leistner, S. Chand, A. Kumar, K. Kamasamudram, N. W. Currier, A. Yezerets and L. Olsson, *Catal. Sci. Technol.*, 2016, **6**, 2565–2579.
32 K. Jisa, J. Novakova, M. Schwarze, A. Vondrova, S. Sklenak and Z. Sobalik, *J. Catal.*, 2009, **262**, 27–34.
33 M. Tamura, K. Shimizu and A. Satsuma, *Appl. Catal., A*, 2012, **433–434**, 135–145.
34 C. R. Reddy, Y. S. Bhat, G. Nagendrappa and B. S. Jai Prakash, *Catal. Today*, 2009, **141**, 157–160.
35 G. Delahay, D. Valade, A. Guzmán-Vagas and B. Coq, *Appl. Catal., B*, 2005, **55**, 149–155.
36 M. Mauvezin, G. Delahay, B. Coq, S. Kieger, J. C. Jumas and J. Olivier-Fourcade, *J. Phys. Chem. B*, 2001, **105**, 928–935.
37 P. S. Miedema and F. M. F. De Groot, *J. Electron Spectrosc. Relat. Phenom.*, 2013, **187**, 32–48.
38 F. M. De Groot, *Coord. Chem. Rev.*, 2005, **249**, 31–63.
39 S. Yang, D. Wang, G. Liang, Y. M. Yiu, J. Wang, L. Liu, X. Sun and T. Sham, *Energy Environ. Sci.*, 2012, **5**, 7007–7016.
40 T. Gu, R. Jin, Y. Liu, H. Liu, X. Weng and Z. Wu, *Appl. Catal., B*, 2013, **129**, 30–38.
41 C. L. Bracey, P. R. Ellis and G. J. Hutchings, *Chem. Soc. Rev.*, 2009, **38**, 2231–2243.
42 L. Lietti, I. Nova, G. Ramis, L. Dall'Acqua, G. Busca, E. Giamello, P. Forzatti and F. Bregani, *J. Catal.*, 1999, **187**, 419–435.
43 X. Li and Y. Li, *J. Mol. Catal. A: Chem.*, 2014, **386**, 69–77.
44 S. Brandenberger, O. Kroecher, A. Wokaun, A. Tissler and R. Althoff, *J. Catal.*, 2009, **268**, 297–306.
45 R. M. Heck, J. M. Chen and B. K. Speronello, *Environ. Prog. Sustainable Energy*, 1994, **13**, 221–225.
46 P. Maitarad, J. Han, D. Zhang, L. Shi, S. Namuangruk and T. Rungrotmongkol, *J. Phys. Chem. C*, 2014, **118**, 9612–9620.
47 M. Devadas, O. Krocher, M. Elsener, A. Wokaun, N. Soger, M. Pfeifer, Y. Demel and L. Mussmann, *Appl. Catal., B*, 2006, **67**, 187–196.
48 J. Eng and C. H. Bartholomew, *J. Catal.*, 1997, **171**, 14–26.
49 M. Wallin, C. J. Karlsson, M. Skoglundh and A. Palmqvist, *J. Catal.*, 2003, **218**, 354–364.
50 M. Iwasaki, K. Yamazaki and H. Shinjoh, *Appl. Catal., A*, 2009, **366**, 84–92.
51 R. Q. Long and R. T. Yang, *J. Catal.*, 2002, **207**, 274–285.
52 P. S. Metkar, N. Salazar, R. Muncrief, V. Balakotaiah and M. P. Harold, *Appl. Catal., B*, 2011, **104**, 110–126.
53 Z. Wu, R. Jin, Y. Liu and H. Wang, *Catal. Commun.*, 2008, **9**, 2217–2220.